RSC Advances

PAPER

View Article Online
View Journal | View Issue

Cite this: *RSC Adv.*, 2024, **14**, 9716

Polyimide-based porous carbon and cobalt nanoparticle composites as high-performance electromagnetic wave absorbers†

Wentao Yu, [a] Jiahui Lin,[a] Zhaozhang Zhao,[a] Jiyong Fang, [b] Ziqing Wang, [c] Jintao Huang *[a] and Yonggang Min *[a]

This study successfully utilized a straightforward approach, choosing liquid–liquid phase separation to build a porous structure and synthesize composite absorbers based on polyimide-based porous carbon and cobalt nanoparticles (designated as PPC/Co-700 and PPC/Co-800). A fine porous structure was achieved as a result of the excellent heat resistance of polyimide resulting in an excellent electromagnetic wave absorption ability of PPC/Co composites. The results obtained clearly indicated that PPC/Co-700 and PPC/Co-800 exhibit a porous structure with coral-like pores, enhancing both impedance matching properties and microwave attenuation abilities. This improvement in impedance matching conditions and dissipation capability is attributed to the synergistic effect of dielectric loss induced by carbon and magnetic loss induced by Co nanoparticles. PPC/Co-700 showed the strongest absorption performance with a minimum reflection loss of −59.85 dB (30 wt% loading, thickness of 3.42 mm) and an effective absorption bandwidth (EABW, RL ≤ −10 dB) of 6.24 GHz (30 wt% loading, thickness of 2.78 mm). Therefore, this work provides a facile strategy for the development of a promising absorbing material with outstanding electromagnetic wave absorption performance.

Received 18th January 2024
Accepted 19th February 2024

DOI: 10.1039/d4ra00488d

rsc.li/rsc-advances

Introduction

The proliferation of electric and electronic technologies and the unbridled usage of electronic gadgets have raised significant concerns due to the resultant electromagnetic wave (EMW) induced pollution.[1–3] Prolonged exposure to EMWs can have deleterious effects on human health and may cause damage to electrical equipment, thereby reducing their operational lifespan.[4] Given the adverse impacts of EMW pollution, there is a rising interest in devising effective methods to mitigate or shield EMW radiation. Particularly, effective EMW shielding can be achieved by utilizing EMW-absorbing materials capable of converting surplus EMW into thermal energy, as opposed to mere reflection.[5,6] This approach helps prevent secondary EMW pollution, making the utilization of EMW-absorbing materials a significant strategy in the realm of EMW protection. As a result, the advancement of EMW-absorbing materials has emerged as a focal point in research within the field of EMW protection.

In general, an excellent EMW absorber is characterized by its strong EMW attenuation ability, wide effective absorbed frequency bandwidth, lightweight construction, and thin thickness, which vary according to the essential application conditions.[7] Numerous compounds can function as ideal EMW-absorbing materials, such as magnetic metals and their alloys (*e.g.*, Fe, Co, Ni),[8–11] ferrite, and its derivatives (*e.g.* Fe_3O_4, $CoFe_2O_4$).[12–15] Over the past few years, there has been a growing interest in carbon materials such as porous carbon,[16,17] carbon fibre (CF),[18,19] and carbon nanotubes (CNT).[20–22] These carbon materials exhibit characteristics distinct from metal composites in electromagnetic wave absorption applications, including lighter weight, higher dielectric loss, and chemical stability. However, to obtain exceptional EMW absorption performance, not only require the presence of strong dielectric loss, but electromagnetic impedance matching conditions is also necessary. Any single carbon material, which rely solely on dielectric loss and exhibit low impedance matching, are not viable options for EMW absorption. Instead, introducing magnetic metal materials into carbon materials to prepare composite materials. It is an effective way to overcome the limitations of carbon-only materials and offer a feasible solution to achieve fine EMW absorption performance. For example, Pan Xu *et al.* designed and synthesized polyetheretherketone-derived hierarchical porous carbon/CoNi bimetallic alloys (HPPPC/CoNi). As a noble EMW absorber, the HPPPC/CoNi demonstrated a minimum RL value of −65.56 at 2.00 mm and

[a]Guangdong University of Technology, Guangzhou 51000, Guangdong, China. E-mail: ygmin@gdut.edu.cn
[b]Midea Corporate Research Cente, Foshan 528000, Guangdong, China
[c]Visionox Technology Co., Ltd, Guangzhou 51000, Guangdong, China

† Electronic supplementary information (ESI) available. See DOI: https://doi.org/10.1039/d4ra00488d

a effective absorption bandwidth of 5.92 GHz at 1.80 mm.[23] Shennan Guo *et al.* prepared iron/cobalt/carbon (Fe/Co/C) nanocomposite fibres (M-CNFs) by using electrospinning and the following heat-treatment method. The sample showed a minimum RL value of −38.1 dB at a matching thickness of 2.5 mm with an effective bandwidth of 4.1 GHz.[24] However, the introduction of magnetic metal materials may cause the increase in the density of the composites and potentially having a negative effect on impedance matching.

The incorporation of a hollow or porous structure in the absorber not only reduces its weight but also enhances its specific surface area and transmission efficiency. Furthermore, the inclusion of low-dielectric air in the material leads to improved impedance matching. Previous studies have extensively explored porous or core–shell structures in this domain.[25–29] Fushan Li prepared a nitrogen-doped porous carbon *via* freeze-dried method[30] and modified nickel nano particles (CN–Ni). The synthesized optimal CN–Ni absorber exhibits excellent EMW absorption performance of an EABW of 5.0 GHz at 2 mm and minimum RL of −43.28 dB. Collectively, the creation of porous structures holds a pivotal role in the performance of EMW absorption. However, the complex design and manufacturing of porous structures have posed challenges to their industrial production. Consequently, there is a crucial requirement to devise a straightforward, and controlled synthetic method for producing carbon/magnetic metal composites with porous or hollow structure as a novel EMW absorber.

The present study describes a facile and efficacious approach for fabricating a porous carbon/cobalt nanoparticle electromagnetic wave absorber using the one-step pyrolysis and liquid–liquid phase separation (LLPS) technique. As the carbon precursor, polyimide (PI) was chosen due to its exceptional thermal stability and facile modification properties, as previously reported.[31–33] In our previous work, we demonstrate that the polyimide-derived porous carbon (PPC) prepared by LLPS maintain its porous structure during pyrolysis method.[34] Herein, to further explore the conformational relationship between the internal crystalline structure and EMW absorbing properties of the fabricated PPC/Co, we change cobalt(III) acetylacetonate as cobalt source; it was added into polyamicacid solution by high-speed stirring to form composite precursor. After LLPS treatment and high-temperature pyrolysis, the porous carbon/cobalt nanoparticle composite absorbers were prepared. The modulation of the internal crystalline structure and EMW absorption properties of PPC/Co were achieved by changing the carbonization temperature. The internal composition, microscopic morphology and EMW absorption capabilities of PPC/Co were systematically characterized. As a remarkable absorber, the structural and compositional advantages of PPC/Co lie their rich pore structure and multiple polarization effect including interface polarization, dipole polarization and defect polarization. Thus, this work offers a straightforward and viable route for the large-scale synthesis of carbon-based EMW absorbers, which can be reproduced with high fidelity.

Experiment

Materials

Dimethylacetamide (DMAC) and cobalt acetylacetonate (III) ($Co(acac)_3$) were supplied by Aladdin Chemistry Co. Ltd and used without further purification. 4,4′-Oxydianiline (ODA) and pyromellitic dianhydride (PMDA) were supplied by Macklin Co. Ltd and used as received. Deionized water was used throughout the experiments.

Synthesis of polyamicacid (PAA) precursor solution

Firstly, 20 g ODA was added into 137 g DMAC and stirred for an hour at 25 °C. Second, 23 g PMDA was slowly added after the diamine had dissolved completely. The solution was stirred at 25 °C for 6 h to obtain PAA precursor solution.

Synthesis of polyimide based porous carbon/cobalt nanoparticles composite (PPC/Co-700, PPC/Co-800)

Typically, polyimide based porous carbon/Cobalt nanoparticles composite were synthesized by the following method: liquid–liquid phase separation to construct porous structures and one-step high temperature pyrolysis to carbonization and introduction Co nanoparticles, as shown in Scheme 1. Firstly, 10.0 g of DMAC and 3.5 g of $Co(acac)_3$ were added to 30.0 g PAA solution and stirred for an hour at 25 °C. Second, the above solution was scraped the film with a coating rod on a glass plate and forms a uniform solution membrane. Then, the obtained solution membrane was immediately immersed in a coagulation bath filled with deionized water at 25 °C for 24 h. Thus, obtained membrane was dried at 70 °C for 24 h. Third, the dried porous PAA membrane was calcined in a tubular furnace under the flow of argon gas under specific heating conditions (imidization: 150 °C/1 h; 250 °C/1 h; 350 °C/1 h. Carbonization: 350–700 °C, 5 °C min^{-1}; 700 °C/1 h). Thus, obtained composites was labelled PPC/Co-700. Additionally, to further explore the impact of carbonization degree on EWM absorption capacity, the membrane was also carbonized at 800 °C and labelled as PPC/Co-800. Besides, to compare the EMW absorption performance changes after introducing cobalt, blank control samples without the introduction of Co nanoparticles were also synthesized following the same synthetic procedure, and the samples were named PPC-700 and PPC-800.

Measurements

The chemical structures of samples were analysed using X-ray powder diffraction (XRD, D/MAX-UltimaIV, Cu Kα, 10–80°, 10° min^{-1}), Raman spectroscopy (LabRAM HR Evolution, 523 nm laser), Fourier transform infrared spectroscopy (FT-IR, Nicolet6700), X-ray photoelectron spectroscopy (Thermo Scientific K-Alpha) and energy-dispersive X-ray spectroscopy (EDS, Oxford X-Max system). The magnetic properties were measured using a vibrating sample magnetometer (VSM, Lake Shore 7404, 298 K). The thermal properties of samples were investigated using thermogravimetric analysis (TGA, PerkinElmer, heating rate: 10 °C min^{-1}; gas flow: 50 ml min^{-1}). The morphology of

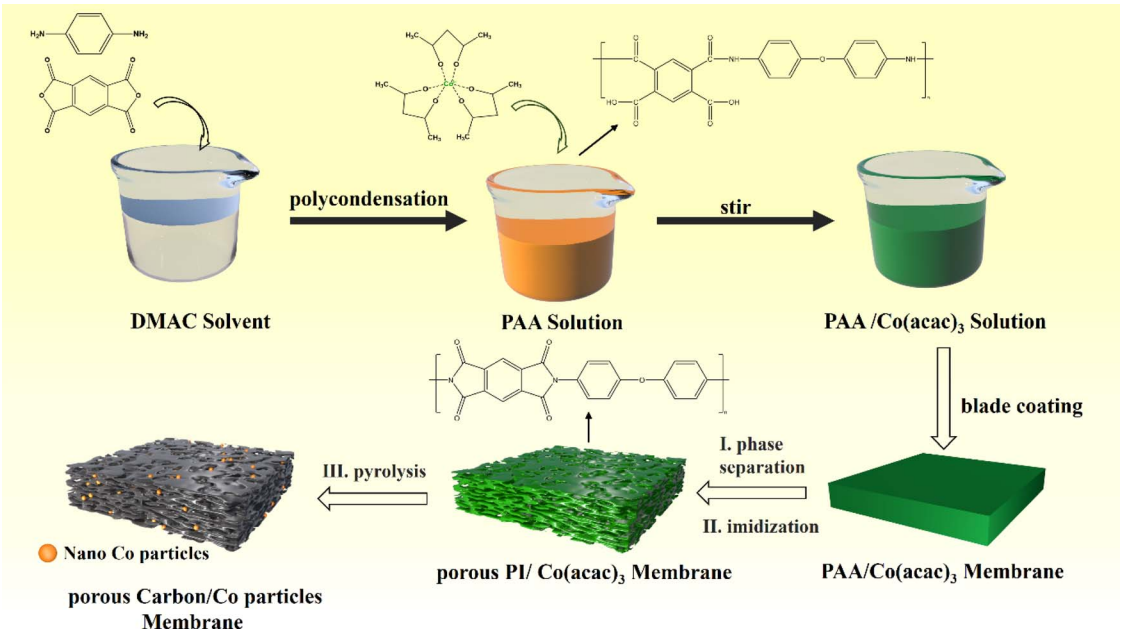

Scheme 1 Synthetic route for the polyimide-based porous carbon/cobalt nanoparticles composite (PPC-700 and PPC/Co-800).

synthesized materials was determined using scanning electron microscopy (SEM, Nova Nano 450). The electromagnetic parameters (complex permeability and permittivity) were measured using a network analyser (N5244A PNA-X, Agilent, toroidal-shaped samples with 30 wt% of products in a paraffin wax matrix, coaxial waveguide method, frequency range: 2–18 GHz).

Results and discussion

Preparation of materials

A one-step strategy has been developed to fabricate a composite electromagnetic wave (EMW) absorber, incorporating polyimide-based porous carbon and cobalt nanoparticles. This method involves the integration of the liquid–liquid phase separation technique with a pyrolysis process. Illustrated in Scheme 1, the synthesis of the porous carbon/magnetic composite entails the use of a porous polymer membrane containing PI as the carbon source and $Co(acac)_3$ as the source of cobalt nanoparticles.

During the imidization, the PAA were confirmed complete conversion to PI according to the FT-IR spectra in Fig. S1.† To verify alterations in the $Co(acac)_3$, the XRD pattern was acquired and presented in Fig. 1(a). Following pyrolysis at 700 °C, the PI underwent carbonization, evident from the detection of a broad diffraction peak at 20–25°, indicating a low degree of graphitization for PI. In the case of PPC/Co-800, the characteristic peaks at 75.90°, 51.36° and 44.12° are associated with the (220), (200) and (111) planes of the face-cantered cubic structure of cobalt nanoparticles (fcc-Co). Therefore, it can be affirmed that the $Co(acac)_3$ underwent chemical reduction to form Co nanoparticles during the carbonization process at 800 °C. Additionally, for PPC/Co-700, the characteristic peaks at 51.36° and 75.90° did not appear in the spectrum, indicating that $Co(acac)_3$ was not completely reduced at 700 °C, which may result in fcc-Co's lattice defects. Moreover, the graphitization peaks in the range of 20–25° are narrower in PPC/Co-800 compared to PPC/Co-700 and PPC-700. This suggests a relatively high degree of graphitization in PPC/Co-800, indicating that cobalt catalysed the crystallization process of polyimide-based carbon. This observation is further supported by the Raman spectra presented in Fig. 1(b). The prominent peaks in the Raman spectra at around 1360 cm^{-1} and 1592 cm^{-1} are attributed to the D and G bands of carbonaceous materials. The intensity ratio of the D/G bands for PPC-700 and PPC/Co-700 is 0.98 and 0.97, respectively. Besides, compared with PPC/Co-700, the PPC/Co-800 had a lower intensity ratio of the D/G bands (0.94), inferring that the intact crystalline phase of fcc-Co can catalyse the graphitization and the result agrees with that obtained from the XRD.

XPS was employed to analyse the surface element composition and valence state of PPC/Co-700. The XPS survey spectrum (Fig. 1(c)) illustrates the presence of C, N, O, and Co elements. The C 1s spectrum in Fig. 1(d) is deconvolved into three peaks, corresponding to C=C (284.9 eV), C–C (285.6 eV) and C=O (289.3 eV) which may cause dipole polarization then improve the EMW absorption. The Co 2p spectrum in Fig. 1(e) is two multi-peaks, corresponding to Co 1/2p and Co 2/3p respectively. Further, the Co 1/2p peak at 778.6 eV and Co 2/3p peak at 796.2 eV are identified as Co^0; the Co $2p_{3/2}$ peak at 780.7 eV and Co $2p_{1/2}$ peak at 799.8 eV are identified as Co^{2+}, which can be attributed to the incomplete decomposition of $Co(acac)_3$, which may cause defect polarization from Co nanoparticles.

To obtain PPC/Co's magnetism, the M–H loops of PPC/Co-700 and PPC/Co-800 were obtained and shown in Fig. 2(b). The S-like shape with nonzero coercivity (H_c) and remanent magnetization (M_r) demonstrated that PPC/Co-700 (M_s = 3.7 emu g^{-1}) and PPC/Co-800 (M_s = 4.5 emu g^{-1}) maintains the super paramagnetic property of the Co nanoparticles. Besides,

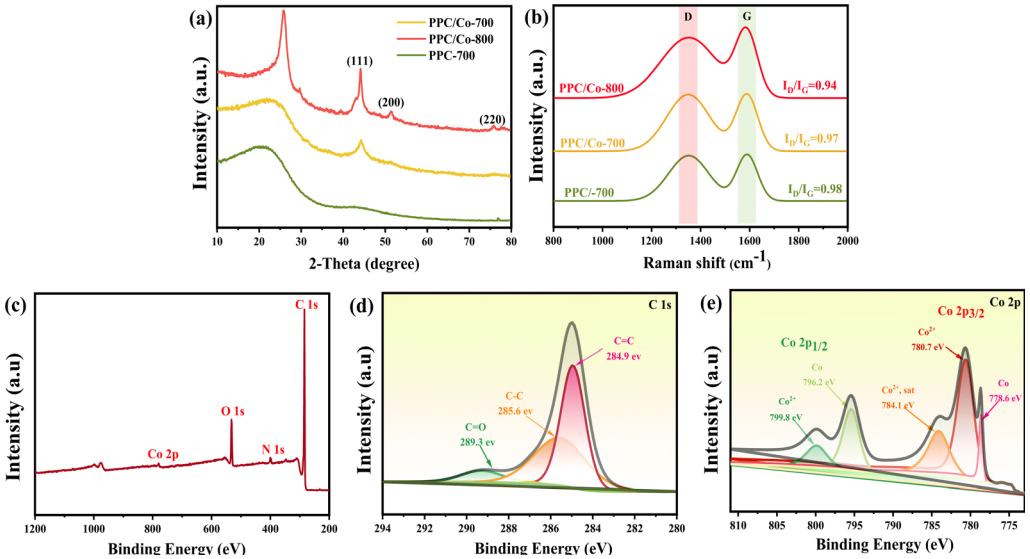

Fig. 1 (a) XRD patterns of PPC-700, PPC/Co-700, and PPC/Co-800; (b) Raman spectra of PPC-700, PPC/Co-700, and PPC/Co-800; (c) XPS survey spectrum of PPC/Co-700; (d) C 1s spectrum; (e) Co 2p spectrum.

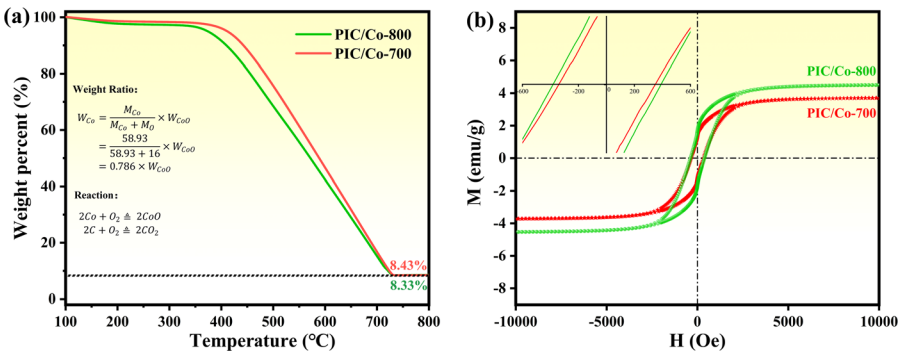

Fig. 2 (a) TGA curves of PPC/Co-700 and PPC/Co-800; (b) M–H loops of PPC/Co-700 and PPC/Co-800.

their low saturation magnetization (M_s) may cause by the low Co metal particles content. As the TGA curves shown at Fig. 2(a), under an air atmosphere, the carbon and Co nano particles in PPC/Co-700 and PPC/Co-800 translates into CO_2 and CoO respectively. The weight ratio of Co particles is calculated as follows:

$$W_{Co} = \frac{M_{Co}}{M_{Co} + M_O} \times W_{CoO} \quad (1)$$

where M_{Co}, M_O represent of Co atom and O atom, respectively; W_{Co} refer to residual weight shown in TGA curves. As the residual weight of PPC/Co-700 and PPC/Co-800 are 8.43% and 8.33%, the Co particles content in PPC/Co-700 and PPC/Co-800 are 6.63% and 6.54% according to the weight ratio equation, respectively.

Morphology and porous structure analysis

The morphology of the as-synthesized PPC-700, PPC/Co-700, and PPC/Co-800 was characterized using scanning electron microscopy, and the results are shown in Fig. 3. As depicted in Fig. 3(a), after undergoing liquid–liquid phase separation, imidization, and carbonization, PPC-700 exhibits well-defined coral-like pores with a pore size ranging from 400 to 900 nm. This suggests the minimal impact of carbonization on the pore structure, attributed to the higher glass transition temperature and thermal degradation temperature of PI, comparing to other polymers. As shown in Fig. 3(b and c), the Co nanoparticles with a size of about 200 nm were randomly dispersed on the surface of the PPC/Co-700 and PPC/Co-800. Further, Fig. 3(d) shows the elemental mapping images of PPC/Co-700. Notably, Co nanoparticles are well-dispersed on the surface of the porous carbon skeleton. Therefore, the SEM analysis can confirm the successful formation of porous PPC and Co nanoparticles composites.

Electromagnetic absorption properties

To clarify the electromagnetic wave (EMW) absorption capabilities of the PPC/Co absorber and the impact of pyrolysis temperature on the EMW absorption properties, the

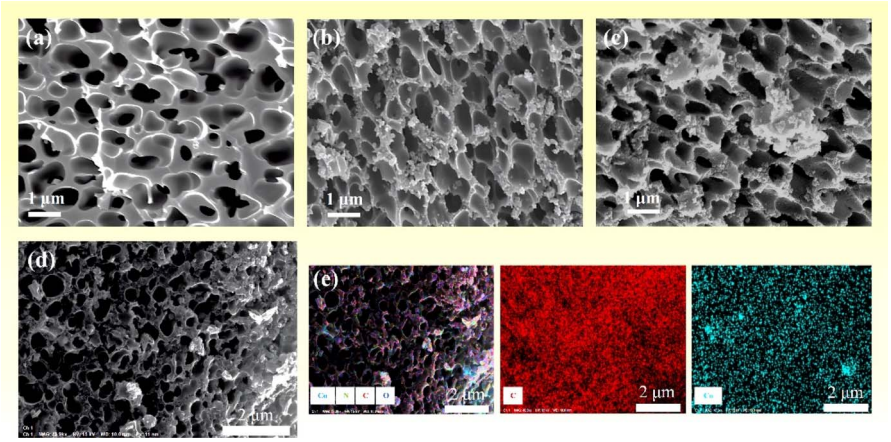

Fig. 3 (a–c) SEM images of PPC-700, PPC/Co-700 and PPC/Co-800; (d and e) elemental mapping images of PPC/Co-700.

electromagnetic parameters of PPC-700, PPC/Co-700 and PPC/Co-800 were assessed using complex permittivity and complex permeability, as illustrated in Fig. 4. The real part (ε', μ') of complex permittivity ($\varepsilon_r = \varepsilon' - i\varepsilon''$), complex permeability ($\mu_r = \mu' - i\mu''$) are associated with the storage capacity of electromagnetic energy, while the imaginary parts (ε'' and μ'') signify the loss of electromagnetic energy.[35] As shown in Fig. 4(a and b), the complex permittivity values of PPC/Co-700, both real and imaginary, were much higher (ε'-8.49–4.02 and ε''-7.04–1.92) than that of PPC-700 (ε'-2.61–2.53 and ε''-0.05–0.11), which was caused by the catalysis of Co nanoparticles. Besides, for PPC/Co-800, the complex permittivity values were higher than PPC/Co-700 as expected, indicating a relatively stronger dielectric loss performance for PPC/Co-800. Meanwhile, Fig. 4 depicts PPC/Co-700 (1.02–0.99, 0.02–0.001) and PPC/Co-800 (1.01–0.97, 0.03–0.001) have weak μ and μ'', respectively. This is due to the low content of cobalt in the PPC/Co absorber.

Dielectric tangent loss ($\tan\delta\varepsilon = \varepsilon''/\varepsilon'$) and magnetic tangent loss ($\tan\delta\mu = \mu''/\mu'$) are common parameters that characterize the dielectric and magnetic loss abilities of EMW absorbers. As depicted in Fig. 4(d–f), the variations in $\tan\delta\varepsilon$ and $\tan\delta\mu$ are closely associated with ε'' and μ'', respectively. Considering the relationship of absorption properties with $\tan\delta\varepsilon$ and $\tan\delta\mu$, higher $\tan\delta\varepsilon$ values imply a significant contribution of dielectric loss to the absorption property in both PPC/Co-700 and PPC/Co-800 samples. Compared to PPC/Co-800 (0.37–0.32), PPC/Co-700 had higher dielectric tangent loss (0.82–0.44), which mean PPC/Co-700 had stronger EMW attenuation capability. However, the role of magnetic cobalt particles as additional promoters for achieving better impedance matching is noteworthy, contributing to the overall EMW absorption performance.

To understand the effect of calcination temperature, the difference between PPC/Co-700 and PPC/Co-800 dielectric loss mechanisms was evaluated using the Cole–Cole plots of two samples, as shown in Fig. 5(a and b). The number of semicircles in the PPC/Co-800 samples is more than that in the PPC/Co-700, suggesting higher conductivity of PPC/Co-800. The higher conductivity is associated with a high degree of graphitization, increasing the dielectric loss. Thus, the conductivity of the composite increased with calcination temperature.

The reflection factor (RL), as a function that can directly characterize the EMW absorption performance of PPC/Co, theoretically derived from obtained electromagnetic parameters. According to the transmission line theory, RL can be calculated using the following eqn (2) and (3).[36]

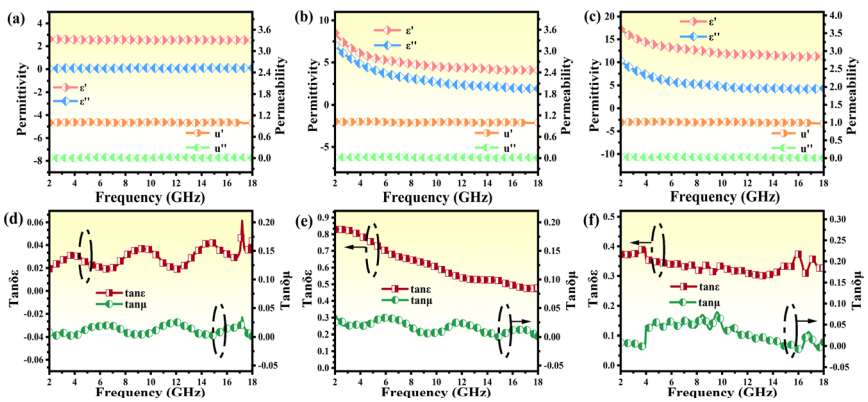

Fig. 4 (a–c) Relative permittivity and permeability for PPC-700, PPC/Co-700 and PPC/Co-800 at 30% absorber content; (d–f) dielectric tangent loss and magnetic tangent loss of PPC-700, PPC/Co-700 and PPC/Co-800 at 30% absorber content.

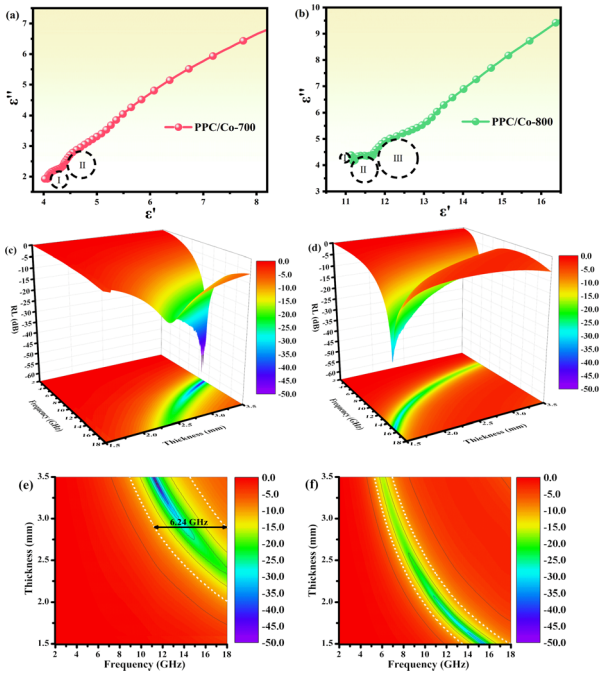

Fig. 5 (a and b) Typical Cole–Cole semicircles ε'' *versus* ε' of PPC/Co-700 and PPC/Co-800; 3D reflection loss and 2D projection plots of PPC/Co-700 (c and e) and PPC/Co-800 (d and f).

$$\mathrm{RL} = 20\lg|(Z_{\mathrm{in}} - Z_0)/(Z_{\mathrm{in}} + Z_0)| \quad (2)$$

$$Z_{\mathrm{in}} = Z_0\sqrt{\mu_{\mathrm{r}}/\varepsilon_{\mathrm{r}}}\tan h\left[j(2\pi fd/c)\sqrt{\mu_{\mathrm{r}}/\varepsilon_{\mathrm{r}}}\right] \quad (3)$$

where Z_{in} represents the equivalent input resistance of the sample; Z_0 represents the impedance of free space, is equal to 377 Ω. The μ_{r} and ε_{r} are the complex permeability and complex permittivity of the sample, and the c is the speed of light in vacuums. f is the frequency and d is the thickness of the specimen.

The RL values and processing results of PPC-700 illustrate almost no absorption ability due to RL values under different thicknesses that are beyond −10 dB (Fig. S2†). By comparison, PPC/Co (PPC/Co-700 and PPC/Co-800) display excellent EMW absorption performance in terms of RL and EABW. PPC/Co-700 with 3.42 mm thickness, has the strongest electromagnetic wave loss ability at 11.44 GHz with a minimum reflection loss ($\mathrm{RL_{min}}$) of −59.85 dB (approximate the 99.9999% EMW absorption), and the effective absorption bandwidth (EABW, the RL ≤ −10 dB, more than 90% EMW absorption) is 5.68 GHz in the frequency range of 17.5–11.76 GHz. Alternatively, the EABW in the frequency range of 17.5–11.76 GHz is 6.24 at the thickness of 2.78 mm, showing a broadband absorption characteristic. Furthermore, PPC/Co-800 (Fig. 5(d and f)) also shows a broadband absorption characteristic that the EABW is 4.40 GHz (17.92–13.52 GHz) at 1.50 mm and $\mathrm{RL_{min}}$ is −34.96 dB at 15.44 GHz. Thus, the incident EMW can be effectively attenuated and transformed into heat and other forms of energy by PPC/Co-700 and PPC/Co-800.

Following the single-layer homogeneous absorber model,[37] the incident electromagnetic wave that is about to come into contact with the surface of the absorber layer has three directions for its electromagnetic energy (E_0) after entering the interior of the absorber layer: part of E_0 reflects on the surface of the layer (air-absorber interface) and returns to the air again the reflected EMW energy on the (E_1); attenuation after entering the interior of absorber the and interacting with it (E_2); and the final EMW energy penetrating the absorber layer and re-reflecting on the surface of the metal layer (the absorber-metal interface (E_3).[38] Specifically, when the absorption layer has an appropriate thickness, *i.e.* a quarter of the incident wavelength frequency, the phase difference between E_1 (incident from air-absorber interface) and E_3 (ejection from absorber-metal interface) is exactly 180°, so the electromagnetic wave energy of the two can nullify each other. This phenomenon is widely known as the quarter-wavelength cancellation model. Consequently, the absorber layer at a specific thickness (t_{m}) can achieve minimal reflection at a certain EMW frequency (f_{m}). The mathematical relationship between t_{m} and f_{m} satisfy the following eqn (4).[39]

$$t_{\mathrm{m}} = \frac{nc}{4f_{\mathrm{m}}\sqrt{|\mu_{\mathrm{r}}||\varepsilon_{\mathrm{r}}|}}(n = 1, 3, 5\ldots) \quad (4)$$

where the f_{m} is the frequency corresponding to obtaining the $\mathrm{RL_{min}}$ value.

The model portrays the inverse relation between the peak frequency and the absorber layer's thickness. As shown in Fig. 6(b and e), it is expected that all thickness related to $\mathrm{RL_{min}}$ value (red symbols) are located around the blue line (the 1/4 wavelength curve of the peak frequency). Consequently, the PPC/Co-700 and PPC/Co-800 based EMW absorber obeys the quarter-wavelength cancellation model, and thus can be concluded that PPC/Co-700 and PPC/Co-800 has considerable contributions to the EMW attenuation performance.

Besides, to obtain the excellent EMW absorption performance, reducing the reflection of EMW (E_1) at the air-absorber interface and improving the absorption of the incident EMW (E_2) in the absorber layer with a low reflection at the absorber-metal interface (E_3) is necessary. The impedance matching characteristics (Z) is an important parameter for reducing the reflection of EMW at the air-absorber interface and is expressed in the following eqn (5)

$$Z = Z_{\mathrm{in}}/Z_0 = \sqrt{\mu_{\mathrm{r}}/\varepsilon_{\mathrm{r}}}\tan h\left[j(2\pi fd/c)\sqrt{\mu_{\mathrm{r}}/\varepsilon_{\mathrm{r}}}\right] \quad (5)$$

The frequency dependence of Z for PPC/Co-700 is shown in Fig. 6(c). At thicknesses of 2.78, 3.11, and 3.42 mm in the absorber layer, Z is almost close to 1 at 14.64, 12.56, and 11.44 GHz, respectively. Simultaneously, these frequencies correspond to the observation of a minimum RL. Interestingly, the porous structures are equivalent to introducing dispersed phases (air) into a continuous phase (carbon), which helps decrease the effective permittivity while balancing permittivity and permeability.[40] Consequently, EMW can easily penetrate the absorber and undergo attenuation rather than reflecting at the absorber surface. Moreover, the well-tuned impedance matching condition of PPC/Co-700 contributes to its outstanding absorbing performance.

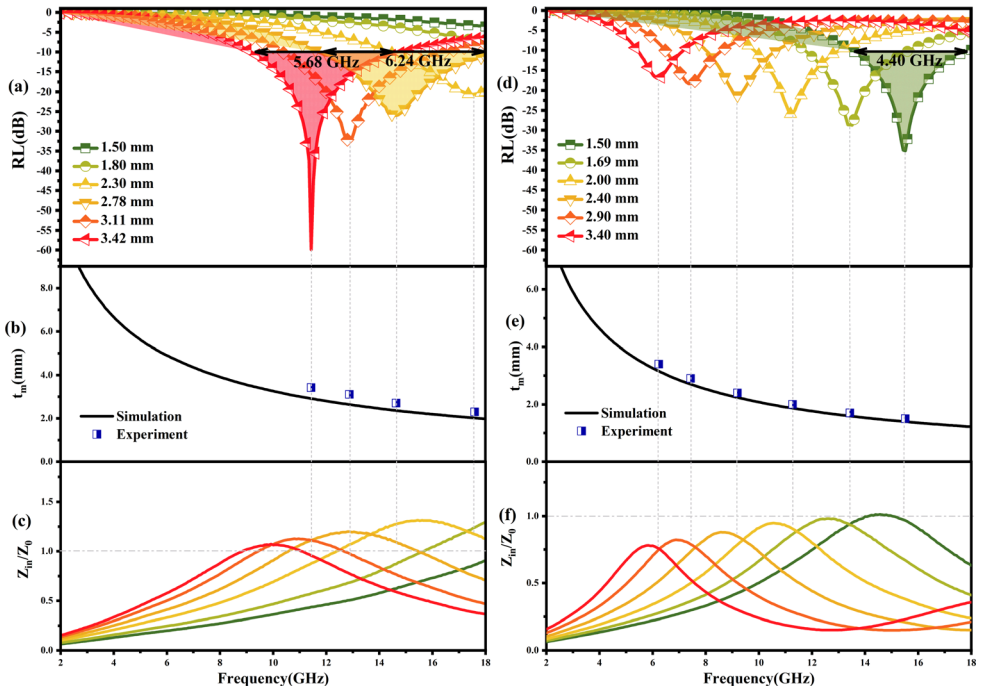

Fig. 6 RL curves with different thicknesses of PPC/Co-700 (a) and PPC/Co-800 (d); simulated and experimental values under 1/4 wavelength matching conditions of PPC/Co-700 (b) and PPC/Co-800 (e); impedance matching characteristics values of PPC/Co-700 (c) and PPC/Co-800 (f).

Shown in Fig. 7, the EMW absorption mechanism of PPC/Co can be explained in the following parts. First, the multiple reflection inside the coral-like pore structure of PPC/Co may result in extended more propagation path for incident EMW, thereby achieving improved EMW attenuation capability of PPC/Co.[41] Second, pore (air), PPC matrix and Co nanoparticles constructs a multiple heterointerfaces, causing strong interface polarization and dielectric relaxation. Additionally, the

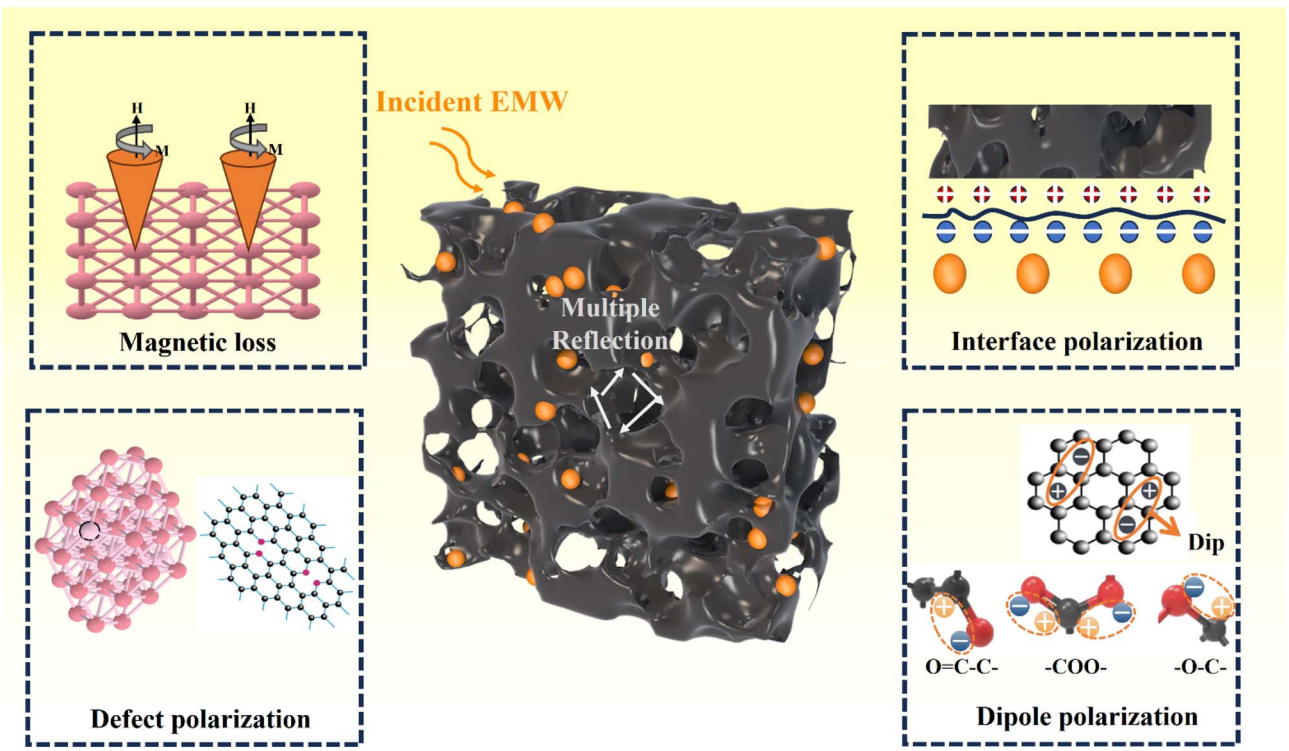

Fig. 7 The schematic presentation of microwave absorbing mechanism of PPC/Co.

Table 1 EMW attenuation performance of representative absorbers and the polyimide-based porous carbon and cobalt nanoparticles composites in this work

Absorber sample	Absorber loading capacity	Magnetic metal load capacity	RL_{min}	EABW	Thickness/mm
PPC/Co-700	30%	6.60%	−59.85	6.24	2.78
PIC/Co-1000[34]	25%	7.15%	−40.22	4.48	5.3
CNF/FeCo[24]	30%	50%	−38.1	4.1	2.5
Co-doped porous carbon/Co[9]	30%	30.40%	−54.5	6.88	2.2
CMT/Co[42]	15%	12.80%	−31.2	5.5	1.4
Co@G NPs[43]	—	80%	−37.7	5.6	5
Co–C@C[44]	25%	32%	−58.1	4.56	2.5

mismatched electronegativity between PPC and Co nanoparticles enhances interface polarization. Third, PPC/Co could effectively reduce EMW reflection due to dipolar polarization and defect polarization triggered by the co-existence of oxygen functional groups, heteroatoms, and lattice defects. Fourth, in addition to dielectric loss, magnetic Co nanoparticles also contribute to natural resonance, exchange resonance, and eddy current effects, enhancing magnetic loss. Table 1 lists some recently developed carbon-based/Co EMW absorbers. Compared with other materials, PPC/Co-700 obtain excellent RL and EABW at a thin thickness, more importantly, PPC/Co-700 can achieve broad absorption at lower magnetic metal load capacity. PPC/Co-700 meet the requirements of lightweight, strong absorption, wider frequency band and easy synthesis for efficiency electromagnetic wave absorbing materials. Therefore, PPC/Co-700 have greater potential for applications in high-performance EMW absorbing materials.

Conclusions

In summary, we successfully utilized a straightforward approach, choosing liquid–liquid phase separation to build a porous structure and synthesize composite absorbers based on polyimide-based porous carbon and cobalt nanoparticles (PPC/Co-700 and PPC/Co-800). The specially designed coral-like pore structures were observed to enhance impedance matching, contribute multiple reflection and strong interfacial polarization, significantly contributes to enhanced EMW absorption. Importantly, the co-exit of cobalt nanoparticles not only induces magnetic loss, but also enhances composite's interface polarization and defeat polarization, and further enhances the EMW attenuation effect of the PPC absorbers through catalytic carbonization degree.

At thicknesses of 2.78 mm and 3.42 mm, PPC/Co-700 achieves minimum RL values of −25.86 dB and −59.86 dB at 14.64 GHz and 11.44 GHz, with EABW of 6.24 GHz and 4.40 GHz. Thus, the design strategy presented in this study could serve as a model for synthesizing other high-performance absorbers, effectively mitigating electromagnetic wave-induced pollution.

Conflicts of interest

There are no conflicts to declare.

Acknowledgements

The authors gratefully acknowledge the National Key R&D Program of China (No. 2020YFB0408100), Guangdong Innovative and Entrepreneurial Research Team Program (No. 2016ZT06C412), National Natural Science Foundation of China (NSFC; No. U20A20340).

References

1 B. Bateer, L. Wang, L. Zhao, P. Yu, C. Tian, K. Pan and H. Fu, *RSC Adv.*, 2015, **5**, 60135–60140.
2 W. X. Li, F. Guo, X. Q. Wei, Y. E. Du and Y. Q. Chen, *RSC Adv.*, 2020, **10**, 36644–36653.
3 Y. Yang, D. Xu, L. Lyu, F. Wang, Z. Wang, L. Wu, W. Liu and J. Liu, *Composites, Part A*, 2021, **142**, 106246.
4 Z. Xu, S. Wang, Y. Xie, Z. Xing, Q. Li, L. Qi, K. Pan and Y. Chen, *J. Alloys Compd.*, 2022, **900**, 163453.
5 Y. Du, *Materials*, 2022, **15**, 1359.
6 W. T. Cao, F. F. Chen, Y. J. Zhu, Y. G. Zhang, Y. Y. Jiang, M. G. Ma and F. Chen, *ACS Nano*, 2018, **12**, 4583–4593.
7 X. J. Zeng, X. Y. Cheng, R. H. Yu and G. D. Stucky, *Carbon*, 2020, **168**, 606–623.
8 N. Poudyal, C. Rong, Y. Zhang, D. Wang, M. J. Kramer, R. J. Hebert and J. Ping Liu, *J. Alloys Compd.*, 2012, **521**, 55–59.
9 B. Wen, H. Yang, Y. Lin, L. Ma, Y. Qiu and F. Hu, *J. Colloid Interface Sci.*, 2021, **586**, 208–218.
10 X. Zeng, C. Zhao, T. Nie, Z. Y. Shen, R. Yu and G. D. Stucky, *Mater. Today Phys.*, 2022, **28**, 100888.
11 Y. Han, M. He, J. Hu, P. Liu, Z. Liu, Z. Ma, W. Ju and J. Gu, *Nano Res.*, 2022, **16**, 1773–1778.
12 H. Wu, J. Liu, H. Liang and D. Zang, *Chem. Eng. J.*, 2020, **393**, 124743.
13 D. Huang, J. Dai, Q. Wang, H. Liu and Z. Li, *J. Alloys Compd.*, 2023, **944**, 169194.
14 Y. Qu, H. Yang, N. Yang, Y. Fan, H. Zhu and G. Zou, *Mater. Lett.*, 2006, **60**, 3548–3552.
15 L. Wang, Z. Ma, H. Qiu, Y. Zhang, Z. Yu and J. Gu, *Micro Nano Lett.*, 2022, **14**, 224.
16 T. Zhao, Z. Jia, Y. Zhang and G. Wu, *Small*, 2023, **19**, e2206323.
17 Z. Wang, Y. Min, J. Fang, W. Yu, W. Huang, X. Lu and B. Wang, *RSC Adv.*, 2023, **13**, 7055–7062.

18 M. Zhang, H. Ling, S. Ding, Y. Xie, T. Cheng, L. Zhao, T. Wang, H. Bian, H. Lin, Z. Li and A. Meng, *Carbon*, 2021, **174**, 248–259.
19 S. Zhang, Z. Jia, Y. Zhang and G. Wu, *Nano Res.*, 2022, **16**, 3395–3407.
20 L. Guo, Y. He, D. Chen, B. Du, W. Cao, Y. Lv and Z. Ding, *Coatings*, 2021, **11**, 534.
21 Y. Zhang, S. Gao, H. Xing and H. Li, *J. Alloys Compd.*, 2019, **801**, 609–618.
22 Y. Zhan, L. Xia, H. Yang, N. Zhou, G. Ma, T. Zhang, X. Huang, L. Xiong, C. Qin and W. Guangwu, *Carbon*, 2021, **175**, 101–111.
23 P. Xu, L. Meng, H. He, D. Qi, S. Wang, J. Fang and X. Yue, *Dalton Trans.*, 2022, **51**, 17430–17440.
24 S. Guo, Y. Zhang, J. Chen, Y. Wu, J. Cao, S. Tang and G. Ji, *Inorg. Chem. Front.*, 2022, **9**, 3244–3250.
25 Y. Ren, Y. Zhang, Q. Zheng, L. Wang and W. Jiang, *Carbon*, 2023, **206**, 226–236.
26 W. Hou, K. Peng, S. Li, F. Huang, B. Wang, X. Yu, H. Yang and H. Zhang, *J. Colloid Interface Sci.*, 2023, **646**, 265–274.
27 D. Fan, B. Wei, R. Wu, J. Zhou and C. Zhou, *J. Mater. Sci.*, 2021, **56**, 6830–6844.
28 H. Wei, H. Wang, A. Li, D. Cui, Z. Zhao, L. Chu, X. Wei, L. Wang, D. Pan, J. Fan, Y. Li, J. Zhang, C. Liu, S. Wei and Z. Guo, *ChemNanoMatc*, 2020, **6**, 174–184.
29 Y. Qiu, Y. Lin, H. Yang, L. Wang, M. Wang and B. Wen, *Chem. Eng. J.*, 2020, **383**, 123207.
30 F. Li, Z. Bi, H. Kimura, H. Li, L. Liu, X. Xie, X. Zhang, J. Wang, X. Sun, Z. Ma, W. Du and C. Hou, *Adv. Compos. Hybrid Mater.*, 2023, **6**, 133.
31 Y. Ma, L. Xu, Z. He, J. Xie, L. Shi, M. Zhang, W. Zhang and W. Cui, *J. Mater. Chem. C*, 2019, **7**, 7360–7370.
32 T. Zhang, Y. Zhao, X. Ma and K. Wang, *Mater. Lett.*, 2021, **300**, 130151.
33 S. Kim, J. Son, H. Park, E. Jeong, K. H. Nam and J. S. Bae, *Polymers*, 2022, **14**, 1425.
34 W. Yu, Y. Min, J. Fang, X. Lu, Z. Wang and L. Jian, *RSC Adv.*, 2022, **12**, 29070–29077.
35 C. Wei, L. Shi, M. Li, M. He, M. Li, X. Jing, P. Liu and J. Gu, *J. Mater. Sci. Nanotechnol.*, 2024, **175**, 194–203.
36 Z. F. Liu, G. Bai, Y. Huang, F. F. Li, Y. F. Ma, T. Y. Guo, X. B. He, X. Lin, H. J. Gao and Y. S. Chen, *J. Phys. Chem. C*, 2007, **111**, 13696–13700.
37 F. Ruiz-Perez, S. M. López-Estrada, R. V. Tolentino-Hernández and F. Caballero-Briones, *J. Sci.: Adv. Mater. Devices*, 2022, **7**, 100454.
38 Z. Yang, M. Li, Y. zhang, L. Yang, J. Liu, Y. Wang and Q. He, *J. Alloys Compd.*, 2020, **817**, 152795.
39 Y. Du, W. Liu, R. Qiang, Y. Wang, X. Han, J. Ma and P. Xu, *ACS Appl. Mater. Interfaces*, 2014, **6**, 12997–13006.
40 Q. Li, J. Liu, Y. Zhao, X. Zhao, W. You, X. Li and R. Che, *ACS Appl. Mater. Interfaces*, 2018, **10**, 27540–27547.
41 Y. Zhu, X. Guan, Z. Yang and X. Xu, *J. Alloys Compd.*, 2021, **865**, 158886.
42 J. Fang, P. Li, Y. Liu and Y. Min, *J. Mater. Chem. C*, 2021, **9**, 2474–2482.
43 X. Shao, T. Wang, Z. Gan, R. Hu, Y. Gong, X. Li, X. Zhang and X. Tian, *Carbon*, 2021, **177**, 171–180.
44 S. Li, L. Lin, L. Yao, H. Zheng, Q. Luo, W. Xu, C. Zhang, Q. Xie, L.-S. Wang and D.-L. Peng, *J. Alloys Compd.*, 2021, **856**, 158183.